ChemComm

COMMUNICATION

View Article Online
View Journal | View Issue



Cite this: *Chem. Commun.*, 2025, **61**, 8723

Received 6th April 2025,
Accepted 10th May 2025

DOI: 10.1039/d5cc01933h

rsc.li/chemcomm



# Constructing nanoneedle arrays of heterostructured $RuO_2$–$Co_3O_4$ with tip-effect-induced enrichment of reactants for enhanced water oxidation†

Xu Zhang,[a] Junnan Song,*[a] Tongming Sun,[b] Minmin Wang,[b] Jinli Zhu,[b] Yang Yu*[c] and Jiacheng Wang*[a]

**Nanoneedle arrays of heterostructured $RuO_2$–$Co_3O_4$ electrocatalysts were constructed, showing improved water oxidation activity and durable stability. The synergy of tip-effect-induced $OH^-$ enrichment, superior hydrophilicity, and heterojunction-enhanced electron transfer promotes water oxidation activity.**

Hydrogen is widely regarded as the most environmentally friendly alternative to fossil fuels. Electrocatalytic water splitting is one of the most promising strategies for sustainable hydrogen production to meet future energy demands.[1] However, the sluggish kinetics of the oxygen evolution reaction (OER) severely hinder the overall efficiency of water splitting.[2] Although Ru-based and Ir-based materials are currently the state-of-the-art OER catalysts, their high cost and natural scarcity present significant barriers to industrial-scale implementation.[3,4] This challenge highlights the urgent need to develop OER catalysts that combine high efficiency, long-term stability, and economic viability.

Notably, heterointerface engineering enables precise tuning of catalyst electronic configurations, optimal modulation of intermediate adsorption strength, and consequent activity enhancement.[5] For example, Mu *et al.* reported that defective $RuO_2/TiO_2$ nanoheterostructures provide 10 mA $cm^{-2}$ at an overpotential of 296 mV for the alkaline OER.[6] Sun *et al.* reported a rutile-structured Ru–Sn solid-solution oxide ($Ru_{0.6}Sn_{0.4}O_2$) displaying a low overpotential of 245 mV to reach 10 mA $cm^{-2}$ in 1.0 M KOH electrolyte.[7] Additionally, the construction of nanoneedle arrays provides dual functional benefits: (1) improving hydrophilicity to accelerate mass transport processes,[8] and (2) obtaining high-curvature nanostructures with tip-enhanced local electric fields that concentrate electrolyte ions and reactants at active sites. This combined effect simultaneously reduces reaction barriers and facilitates rapid mass transfer to active sites, ultimately boosting catalytic activity.[9] Thus, it is expected that high-performance $RuO_2$-based electrocatalysts could be prepared by integrating heterojunction and morphology engineering. In addition, spinel $Co_3O_4$ with low cost and abundant active sites is considered to be a promising catalyst for the OER, which can improve the activity by adjusting the electronic structure and local structure. Bo and coworkers constructed $Co_3S_4$@$Co_3O_4$/NSC core@shell nanostructures as bifunctional ORR/OER electrocatalysts for rechargeable Zn–air batteries. The interfaces between $Co_3S_4$@$Co_3O_4$ and $Co_3O_4$/NSC could improve conductivity, and accelerate charge transfer.[10] Jin *et al.* developed a heterogeneous $Co_3O_4/CeO_2$ nanocomposite to modify the electronic structure of $Co_3O_4$ and establish an improved local bonding environment by introducing $CeO_2$, consequently modifying the redox characteristics of Co and enhancing the acidic OER performance.[11] Therefore, simply constructing heterojunction structures and focusing on the surface reconstruction between multiple metal oxide surfaces could improve the OER activity for hydrogen economy.

Herein, we synthesized $RuO_2$ nanoparticle-decorated $Co_3O_4$ nanoneedle arrays on nickel foam (NF) through a sequential process involving $Co_3O_4$ growth, $Ru^{3+}$ ion exchange, and subsequent annealing. The resulting $RuO_2/Co_3O_4$ heterostructure exhibits outstanding OER electrocatalytic performance in alkaline media, achieving a low overpotential of 223 mV at 100 mA $cm^{-2}$ with remarkable stability exceeding 100 hours of continuous operation. XPS analysis shows that electrons transfer from $RuO_2$ to $Co_3O_4$ at the heterogeneous interface, resulting in electron redistribution, which can optimize OER energetics. The nanoneedle architecture simultaneously enhances surface hydrophilicity, accelerating mass transport. Furthermore, the densely arranged $Co_3O_4$ nanoneedles bind to enhance the local electric field effect induced by the tip, promoting $OH^-$ enrichment at active sites while exposing additional catalytic centers.

[a] *Zhejiang Key Laboratory for Island Green Energy and New Materials, Institute of Electrochemistry, School of Materials Science and Engineering, Taizhou University, Taizhou 318000, Zhejiang, China. E-mail: jnsong@nuaa.edu.cn, jiacheng.wang@tzc.edu.cn*

[b] *College of Chemistry and Chemical Engineering, Nantong University, Nantong 226019, Jiangsu, China*

[c] *School of Pharmaceutical Sciences, Taizhou University, Taizhou 318000, Zhejiang, China. E-mail: yuyang430@tzc.edu.cn*

† Electronic supplementary information (ESI) available. See DOI: https://doi.org/10.1039/d5cc01933h

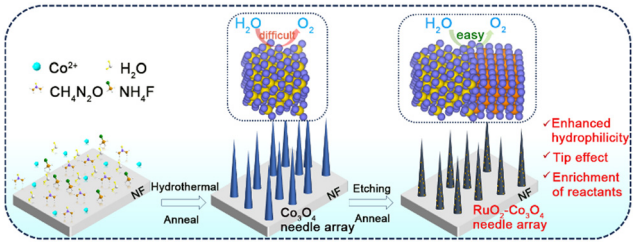


Fig. 1 Schematic drawing of heterostructured $RuO_2/Co_3O_4$ needle-array electrocatalysts for efficient OER.

This dual mechanism facilitates efficient $O_2$ evolution and significantly enhances alkaline OER kinetics. Our findings provide fundamental insights into the electronic structure modulation of heterostructured catalysts and contribute to the development of cost-effective catalytic systems for practical water electrolysis.

Fig. 1 shows the decoration of $Co_3O_4$ nanoneedle arrays with $RuO_2$ nanoparticles. The synthesis begins with the thermal conversion of cobalt carbonate hydroxide (CoCH) into a $Co_3O_4$ scaffold structure. Subsequently, the obtained $Co_3O_4$ substrates undergo controlled ion exchange reactions in an aqueous $RuCl_3$ solution for varying durations, followed by calcination under ambient conditions to produce the final $RuO_2/Co_3O_4$ electrocatalyst. Dynamic contact angle measurements (Fig. S1, ESI†) reveal the superior hydrophilicity of the $RuO_2/Co_3O_4$ electrocatalyst compared to bare NF. Upon water droplet contact ($t$ = 0 s), complete surface wetting occurred within 0.073 seconds for the composite catalyst, demonstrating rapid electrolyte penetration, which facilitates optimal electrode–electrolyte interfacial contact. In addition, the rough nanoneedles formed by loaded nanoparticles can cause sharp tip enhancement and proximity effects, and generate stronger electric fields, which are conducive to the enrichment of $OH^-$ around the active site, optimizing the reaction energy barrier, and promoting the release of $O_2$ bubbles, thereby improving the OER process.[12]

The surface morphology of the catalysts was examined using field-emission scanning electron microscopy (FESEM). The as-prepared CoCH precursor exhibited smooth nanoneedle-like structures with a diameter of approximately 3–4 μm (Fig. S2, ESI†). After calcination to form $Co_3O_4$, the nanoneedle architecture remained largely intact (Fig. S3, ESI†). Subsequent $Ru^{3+}$ ion exchange followed by calcination produced $RuO_2/Co_3O_4$ heterostructures, which preserved the nanoneedle morphology while exhibiting uniformly anchored $RuO_2$ nanoparticles on the surface, resulting in a roughened nanostructure (Fig. 2a–c). This well-defined nanoneedle configuration maximizes the exposure of active sites, enhances electrolyte infiltration, facilitates bubble release, and ensures structural stability during prolonged oxygen evolution reaction (OER).[13]

Transmission electron microscopy (TEM) further confirmed the unique nanowire-like structure of $RuO_2/Co_3O_4$ (Fig. 2d). High-resolution TEM (HRTEM) analysis revealed lattice spacings of 0.28 nm and 0.31 nm (Fig. 2e), corresponding to the (220) plane of $Co_3O_4$ and the (110) plane of $RuO_2$, respectively. High-angle annular dark-field TEM (HAADF-TEM) imaging, coupled with

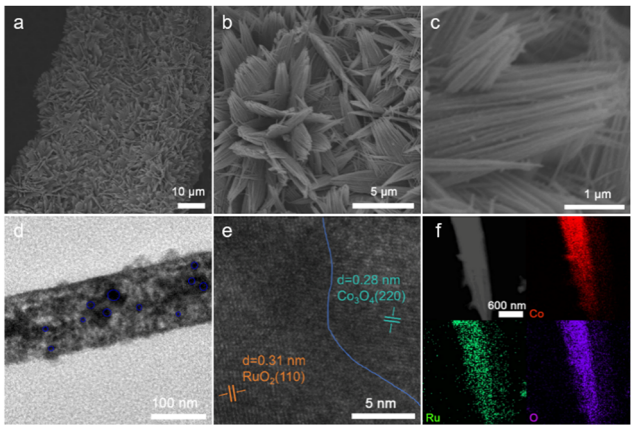


Fig. 2 (a)–(c) SEM, (d) TEM, (e) HRTEM, and (f) EDX mapping images of $RuO_2/Co_3O_4$ needle-arrays.

elemental mapping (Fig. 2f), demonstrated the homogeneous spatial distribution of Ru, Co, and O throughout the whole needle, conclusively verifying the formation of $RuO_2/Co_3O_4$ heterogeneous nanoneedles.

The heterostructure of $RuO_2/Co_3O_4$ was analyzed using X-ray diffraction (XRD, Fig. 3a). It shows distinct diffraction peaks at 31.2°, 36.8°, 44.8°, 59.3°, and 65.2°, corresponding to the (220), (311), (400), (511), and (440) planes of cubic $Co_3O_4$ (JCPDS no. 09-0418). Additional peaks at 28.0°, 35.0°, and 54.3° align with the (110), (101), and (211) planes of tetragonal $RuO_2$ (JCPDS no. 43-1027), confirming the successful formation of the heterostructure.

The electronic structure of $RuO_2/Co_3O_4$ was investigated by X-ray photoelectron spectroscopy (XPS, Fig. 3b). In the Co 2p XPS spectra (Fig. 3c), two significant peaks of pristine $Co_3O_4$ located at 779.3 and 794.3 eV belong to $Co^{3+}$, while another two peaks positioned at 780.5 and 795.5 eV are attributed to $Co^{2+}$. In the spinel structure of $Co_3O_4$, $Co^{2+}$ is located at a tetrahedral position, while $Co^{3+}$ cations are located in octahedral sites.[14] Compared to $Co_3O_4$, the binding energies of $RuO_2/Co_3O_4$ exhibit a negative shift of *ca.* 0.5 eV. As displayed in Fig. 3d,

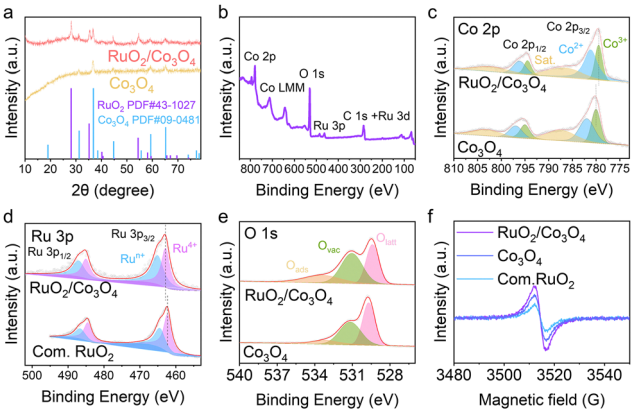


Fig. 3 (a) XRD patterns of $RuO_2/Co_3O_4$ and $Co_3O_4$. (b) The whole XPS spectrum of $RuO_2/Co_3O_4$. (c)–(e) The XPS spectra of (c) Co 2p, (d) Ru 3p, and (e) O 1s for $RuO_2/Co_3O_4$. (f) Electron paramagnetic resonance of $RuO_2/Co_3O_4$, com. $RuO_2$ and $Co_3O_4$.

 

the Ru 3p XPS spectra show two pairs of spin–orbit double peaks located at around 462.9 and 465.1 eV for Ru $3p_{3/2}$ and 485.1 and 487.2 eV for Ru $3p_{1/2}$, which are assigned to the $Ru^{4+}$ and $Ru^{>4+}$ species.[15] Compared to commercial $RuO_2$, the binding energies of $RuO_2/Co_3O_4$ exhibit a positive shift of *ca.* 0.6 eV, implying a partial charge transfer between $RuO_2$ and $Co_3O_4$, which can be attributed to the strong support and active phase synergy effect. Deconvolution of the O 1s spectra (Fig. 3e) identifies three components: lattice oxygen ($O_{latt}$, 529.3 eV), oxygen vacancies ($O_{vac}$, 531.0 eV), and adsorbed water ($O_{ads}$, 533.4 eV).[16] Among them, the oxygen vacancy content of $RuO_2/Co_3O_4$ increased by 4% compared with cobalt tetroxide. This result is confirmed by the electron paramagnetic resonance (EPR) spectrum (Fig. 3f). This vacancy enrichment likely originates from charge compensation during $Ru^{3+}$ ion exchange. Collectively, these results demonstrate significant electronic restructuring at the $RuO_2/Co_3O_4$ interface. The synergistic interaction between the phases can optimize the water dissociation kinetics and intermediate adsorption/desorption energetics, thereby accelerating overall water electrolysis efficiency.[17]

The OER activity of $RuO_2/Co_3O_4$ was systematically evaluated in 1 M KOH using a conventional three-electrode system, with comparative studies against pristine $RuO_2/Co_3O_4$ and commercial $RuO_2$. Linear sweep voltammetry (LSV) curves were *iR*-corrected and normalized to the reversible hydrogen electrode (RHE). The Ru content in $RuO_2/Co_3O_4$ was precisely controlled by varying ion-exchange durations, with inductively coupled plasma optical emission spectrometer (ICP-OES) analysis confirming the optimized mass ratio (Table S1, ESI†). After 9 hours of ion exchange, the catalyst exhibited peak performance, characterized by a high electrochemical active surface area (ECSA) and low charge-transfer resistance (Fig. S4 and S5, ESI†). As illustrated in Fig. 4a, $RuO_2/Co_3O_4$ requires an exceptionally low overpotential of 223 mV to deliver 100 mA $cm^{-2}$, significantly surpassing $RuO_2/Co_3O_4$ (350 mV) and commercial $RuO_2$ (400 mV). Impressively, even at a high current density of 200 mA $cm^{-2}$, $RuO_2/Co_3O_4$ maintains superior performance with minimal overpotential (Fig. 4b), outperforming benchmark catalysts across all tested current densities. Reaction kinetics analysis reveals a Tafel slope of 46.46 mV $dec^{-1}$ for $RuO_2/Co_3O_4$, markedly lower than $Co_3O_4$ (70.66 mV $dec^{-1}$) and commercial $RuO_2$ (87.63 mV $dec^{-1}$) (Fig. 4c), confirming accelerated OER kinetics enabled by heterointerface engineering. Electrochemical impedance spectroscopy (EIS) further corroborates this enhancement, with $RuO_2/Co_3O_4$ exhibiting the smallest semicircle diameter (Fig. 4d), indicative of reduced charge-transfer resistance and faster interfacial kinetics. The ECSA, derived from double-layer capacitance ($C_{dl}$) measurements *via* cyclic voltammetry at varying scan rates (Fig. S6, ESI†), reaches 328.95 mF $cm^{-2}$ for $RuO_2/Co_3O_4$, exceeding $Co_3O_4$ (167.60 mF $cm^{-2}$) and commercial $RuO_2$ (40.68 mF $cm^{-2}$) by factors of 1.96 and 8.09, respectively (Fig. 4e).[18] This substantial increase in $C_{dl}$ directly correlates with electronic structure modulation at the $RuO_2/Co_3O_4$ heterointerface, which exposes abundant active sites and enhances charge-transfer efficiency.

The enhanced electrocatalytic activity may be attributed to the tip effect of the rough nanoneedles.[12] Densely packed

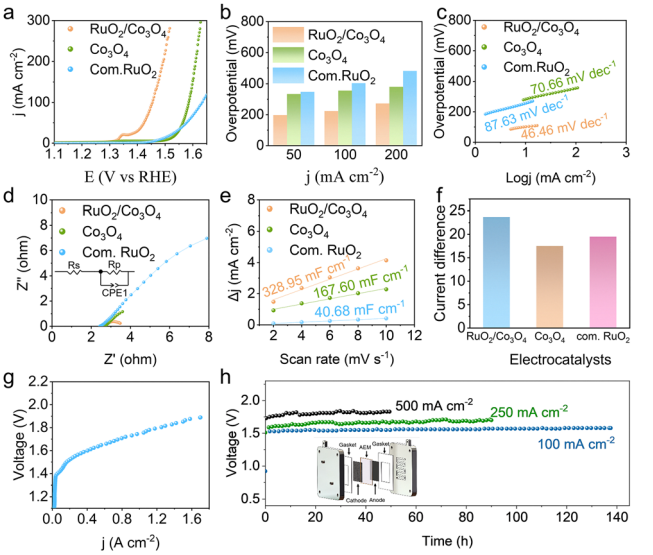


Fig. 4 (a) LSV curves, (b) overpotentials at 50, 100 and 200 mA $cm^{-2}$, (c) corresponding Tafel slopes, (d) EIS Nyquist plots, and (e) capacitive current density against the scan rate of $RuO_2/Co_3O_4$, $Co_3O_4$, and com. $RuO_2$ in 1.0 M KOH. (f) Current difference between the polarization curves in 1.0 M KOH solution with and without 1.0 M methanol for $RuO_2/Co_3O_4$, $Co_3O_4$ and com. $RuO_2$. (g) Polarization curves of $RuO_2/Co_3O_4$, which were measured by the use of an AEMWE cell in 1.0 M KOH with a scan rate of 10 mV $s^{-1}$. (h) Chronopotentiometric measurements of stability at 0.5 A $cm^{-2}$, 0.25 A $cm^{-2}$ and 0.1 A $cm^{-2}$. Inset is a diagram of an AEMWE electrolyzer.

nanoneedles can induce a strong local electric field, enriching $OH^-$ ions at the electrode surface, exposing more active sites to $OH^-$ ions, and promoting $O_2$ release, thus accelerating the alkaline oxygen evolution reaction (OER) process. To verify the enrichment of $OH^-$ ions, methanol molecular probe experiments were conducted (Fig. S7, ESI†). The methanol oxidation reaction (MOR) follows a well-established mechanism in which methanol molecules nucleophilically attack electrophilic *OH species.[19,20] The nucleophilic reagent methanol can easily adsorb the electrophilic reagent *OH in the process of the OER, which forms a competitive relationship with the adsorption of *OH by the OER. Therefore, the MOR is considered as an electronic probe assaying the adsorption of OER intermediates, that is, the increase of current density in the MOR is positively correlated with the coverage of intermediate *OH.[21,22] The difference in current density due to the MOR is proportional to the charge transferred, which can be quantified by calculating the area between the curves (Fig. 4f). The current difference between the MOR and OER on $RuO_2/Co_3O_4$ nanoneedles is greater than that observed on $Co_3O_4$ and $RuO_2$, indicating a stronger MOR competitive reaction and validating enhanced *OH adsorption on $RuO_2/Co_3O_4$. To demonstrate the stability of $RuO_2/Co_3O_4$ in an alkaline environment, the catalyst stability was tested at a current density of 100 mA $cm^{-2}$. The voltage degradation of $RuO_2/Co_3O_4$ was found to be negligible after 100 hours (Fig. S8, ESI†).

After the OER stability test, a series of characterizations were executed to minutely explore the morphology or structure evolutions of the spent catalyst. XPS was also carried out to

investigate the chemical state and surface composition of the oxide after the stability test (Fig. S9, ESI†). It can be seen that the binding energy of Ru 3p has undergone a slight positive shift, indicating that Ru has undergone a slight oxidation during the OER process. SEM analysis was used to observe micro-morphological changes after testing, revealing that the nanowire array remained largely intact and that Ru, Co, and O elements were uniformly distributed throughout the catalyst (Fig. S10, ESI†), highlighting the robustness of the catalyst. Notably, the OER performance of $RuO_2/Co_3O_4$ outperforms most recently reported Ru-containing electrocatalysts (Fig. S10 and Table S2, ESI†). In addition, we used custom anion exchange membrane electrolysis (AEMWE) cells to evaluate water decomposition performance in alkaline media with high current density. Under continuous operation, the $RuO_2/Co_3O_4$ based AEMWE only needs 1.723 V battery voltage to achieve 1 A $cm^{-2}$ water decomposition current density (Fig. 4g). To assess its industrial relevance, extended stability tests were performed at current densities of 0.1, 0.25, and 0.5 A $cm^{-2}$ (Fig. 4h). The cell demonstrated excellent long-term stability, with negligible voltage fluctuations during 120 hours of operation, confirming the structural integrity and corrosion resistance of the $RuO_2/Co_3O_4$ catalyst under harsh alkaline conditions. These results suggest that $RuO_2/Co_3O_4$ exhibits excellent OER activity and significant stability due to the presence of abundant heterogeneous interfaces and densely packed nanoneedles.

In summary, we have developed highly efficient and stable $RuO_2/Co_3O_4$ heterogeneous nanoneedle electrocatalysts through an ion exchange reaction and a simple pyrolysis method. The optimal $RuO_2/Co_3O_4$ electrocatalyst achieves a minimal overpotential of 223 mV at 100 mA $cm^{-2}$. Furthermore, it exhibits exceptional OER stability, with no significant degradation observed at 100 mA $cm^{-2}$ over 100 hours, outperforming most recently reported state-of-the-art electrocatalysts. The experimental results demonstrate that the heterogeneous interface facilitates strong electron interactions, enhancing the OER activity. Additionally, the methanol oxidation molecular probe test confirms that the densely packed nanoneedles promote the enrichment of $OH^-$ ions around the active sites, exposing more active sites to $OH^-$ ions, thereby accelerating the release of $O_2$ bubbles. This study presents a viable approach for producing high-performance transition metal oxide catalysts for efficient water oxidation.

The authors are grateful for the financial support from the National Natural Science Foundation of China (52472231, 52311530113, W2521017) and the Central Guidance on Science and Technology Development Fund of Zhejiang Province (2024ZY01011).

## Data availability

Data available within the article or its ESI.†

## Conflicts of interest

There are no conflicts to declare.

## Notes and references

1 J. Huang, B. Hu, J. Meng, T. Meng, W. Liu, Y. Guan, L. Jin and X. Zhang, *Energy Environ. Sci.*, 2024, **17**, 1007–1045.
2 H. Liu, W. Shen, H. Jin, J. Xu, P. Xi, J. Dong, Y. Zheng and S.-Z. Qiao, *Angew. Chem., Int. Ed.*, 2023, **62**, e202311674.
3 T. Jin, S. Shen, A. Xu, J. Pan, G. Zhou and W. Zhong, *Small*, 2025, **21**, 2500667.
4 Z. Yan, Z. Liu, G. Zhou, T. Jin, H. Zhang, L. Gu, T. Gao, S. Shen and W. Zhong, *Angew. Chem., Int. Ed.*, 2025, **137**, e202501964.
5 H. Du, T. Sun, M. Wang, Y. Tang, Y. Yu and J. Wang, *Chem. Commun.*, 2025, **61**, 5719–5730.
6 W. Li, H. Zhang, M. Hong, L. Zhang, X. Feng, M. Shi, W. Hu and S. Mu, *Chem. Eng. J.*, 2022, **431**, 134072.
7 S. Jia, J. Zhang, Q. Liu, C. Ma, Y. Tang and H. Sun, *J. Mater. Chem. A*, 2023, **11**, 23489–23497.
8 F. He, Y. Mao, Y. Hu, J. Wu, E. Xie, Z. Wang and Y. Li, *Chem. Commun.*, 2024, **60**, 11347–11350.
9 P. Liu, B. Chen, C. Liang, W. Yao, Y. Cui, S. Hu, P. Zou, H. Zhang, H. J. Fan and C. Yang, *Adv. Mater.*, 2021, **33**, 2007377.
10 C. Guo, Y. Zhang, M. Yin, J. Shi, W. Zhang, X. Wang, Y. Wu, J. Ma, D. Yuan and C. Jia, *J. Power Sources*, 2021, **485**, 229315.
11 J. Huang, H. Sheng, R. D. Ross, J. Han, X. Wang, B. Song and S. Jin, *Nat. Commun.*, 2021, **12**, 3036.
12 P. Ye, K. Fang, H. Wang, Y. Wang, H. Huang, C. Mo, J. Ning and Y. Hu, *Nat. Commun.*, 2024, **15**, 1–12.
13 M. Gao, J. Li, Z. Wang, Z. Yang, Y. Chen, W. Deng, W. Liang, T. Ao and W. Chen, *Sep. Purif. Technol.*, 2024, **328**, 125084.
14 R. Zhang, L. Pan, B. Guo, Z.-F. Huang, Z. Chen, L. Wang, X. Zhang, Z. Guo, W. Xu, K. P. Loh and J.-J. Zou, *J. Am. Chem. Soc.*, 2023, **145**, 2271–2281.
15 J. Wang, W. He, Y. Zong, Y. Tang, J. Wang and R. Ma, *Chem. Commun.*, 2024, **60**, 9444–9447.
16 Y. Feng, X. Wang, J. Ma, N. Wang, Q. Liu, K. Suenaga, W. Chen, J. Zhang, Y. Zhou and J. Wang, *Adv. Energy Mater.*, 2024, **14**, 2401501.
17 Y. Feng, N. Ran, X. Wang, Q. Liu, J. Wang, L. Liu, K. Suenaga, W. Zhong, R. Ma and J. Liu, *Adv. Energy Mater.*, 2023, **13**, 2302452.
18 H. Zhu, J. J. Wang, Z. Xu, Y. Tan and J. Wang, *Small*, 2024, **20**, 2404919.
19 Y. Qi, Y. Zhang, L. Yang, Y. Zhao, Y. Zhu, H. Jiang and C. Li, *Nat. Commun.*, 2022, **13**, 4602.
20 L. Li, G. Zhang, C. Zhou, F. Lv, Y. Tan, Y. Han, H. Luo, D. Wang, Y. Liu, C. Shang, L. Zeng, Q. Huang, R. Zeng, N. Ye, M. Luo and S. Guo, *Nat. Commun.*, 2024, **15**, 4974.
21 H. B. Tao, Y. Xu, X. Huang, J. Chen, L. Pei, J. Zhang, J. G. Chen and B. Liu, *Joule*, 2019, **3**, 1498–1509.
22 Y. Mei, J. Chen, Q. Wang, Y. Guo, H. Liu, W. Shi, C. Lin, Y. Yuan, Y. Wang, B. Y. Xia and Y. Yao, *Sci. Adv.*, 2024, **10**, eadq6758.

 